nature geoscience

ARTICLES

https://doi.org/10.1038/s41561-019-0466-8

Global cooling linked to increased glacial carbon storage via changes in Antarctic sea ice

Alice Marzocchi[1]* and Malte F. Jansen[2]

Palaeo-oceanographic reconstructions indicate that the distribution of global ocean water masses has undergone major glacial–interglacial rearrangements over the past ~2.5 million years. Given that the ocean is the largest carbon reservoir, such circulation changes were probably key in driving the variations in atmospheric CO_2 concentrations observed in the ice-core record. However, we still lack a mechanistic understanding of the ocean's role in regulating CO_2 on these timescales. Here, we show that glacial ocean–sea ice numerical simulations with a single-basin general circulation model, forced solely by atmospheric cooling, can predict ocean circulation patterns associated with increased atmospheric carbon sequestration in the deep ocean. Under such conditions, Antarctic bottom water becomes more isolated from the sea surface as a result of two connected factors: reduced air–sea gas exchange under sea ice around Antarctica and weaker mixing with North Atlantic Deep Water due to a shallower interface between southern- and northern-sourced water masses. These physical changes alone are sufficient to explain ~40 ppm atmospheric CO_2 drawdown—about half of the glacial–interglacial variation. Our results highlight that atmospheric cooling could have directly caused the reorganization of deep ocean water masses and, thus, glacial CO_2 drawdown. This provides an important step towards a consistent picture of glacial climates.

Since the onset of the Northern Hemisphere glaciation (~2.7 million years ago), Earth's climate has undergone large transitions between cold glacial and warm interglacial (for example, present-day) stages. The geological record suggests that such transitions were also accompanied by large-scale ocean circulation changes, which were probably key in the glacial–interglacial shifts themselves, by affecting the partitioning of carbon between the atmosphere and the ocean[1,2].

The distribution of carbon, heat and freshwater throughout the global ocean is largely shaped by the meridional overturning circulation, which today consists of two main overturning cells that originate in the polar regions. The upper cell, or Atlantic meridional overturning circulation (AMOC), is associated with sinking of dense water to depths of ~3 km in the subpolar North Atlantic, and the abyssal cell is fed by the formation of even denser water around Antarctica. Antarctic bottom water (AABW) formation and wind-driven upwelling of deep waters originating from both hemispheres make the Southern Ocean the dominant conduit for the exchange of heat and carbon between the surface and the abyss[3].

The leading interpretations of geochemical water mass tracers indicate that ocean circulation was substantially different during the Last Glacial Maximum (LGM, ~21,000 years ago) and characterized by a shallower AMOC[4–6]. The glacial deep ocean was not only colder, but also probably more stratified and saltier[7,8]. The interpretation of many of these reconstructions is, however, still debated[9]. To further complicate matters, the representation of the glacial ocean state in coupled climate simulations differs substantially between models and is often at odds with the geological evidence[10–12].

A number of studies have highlighted the key role of Antarctic sea ice and the resulting surface buoyancy forcing in driving the inferred glacial–interglacial rearrangements in global ocean water masses[13–21]. A recent study directly linked glacial circulation changes to atmospheric cooling[18], suggesting that enhanced brine rejection from Antarctic sea ice formation in a colder climate leads to increased abyssal stratification and ultimately a shoaling of the AMOC[22]. Coupled climate models simulating strong LGM sea ice formation have also been shown to exhibit enhanced stratification and a shallower AMOC, largely consistent with the geological evidence, while LGM simulations with relatively little Antarctic sea ice typically reveal the opposite response[12].

Given that the ocean is the largest carbon reservoir that reacts on glacial–interglacial timescales, the suggested changes in ocean circulation may play an important role in explaining the variations in atmospheric CO_2 concentrations between glacial and interglacial climates[1,2]. Several modelling studies have investigated the ocean's role in glacial–interglacial changes in carbon storage[23–29], but no consensus has yet been reached on which are the dominant drivers and processes. The existing studies typically use models with highly simplified physics, coarse resolution, and/or a complex coupling between the atmosphere, sea ice and ocean components. In addition, physical and biogeochemical drivers have often been considered in conjunction, which makes it difficult to disentangle the response to a number of changes in the boundary conditions and to obtain a deeper mechanistic understanding of the results.

Here, we apply an idealized yet physically robust set-up, using an ocean–sea ice general circulation model (GCM), where changes in the ocean circulation and biogeochemistry are forced solely by atmospheric cooling (see Methods). The physical changes between a warm (interglacial) and cold (glacial) climate are described in a previous manuscript[18] and are broadly consistent with the available LGM proxy record. The model set-up uses an idealized geometry, which includes only one ocean basin, but simulations with multiple ocean basins and more complex coupled climate models suggest that the idealized model reproduces the global mean meridional overturning circulation changes found in multi-basin models[12,21]. In this study, we also include a biogeochemical model with a closed carbon cycle to gain a mechanistic understanding of the role of the physical changes in regulating glacial atmospheric CO_2.

[1]National Oceanography Centre, Southampton, UK. [2]Dept. of the Geophysical Sciences, The University of Chicago, Chicago, IL, USA.
*e-mail: alice.marzocchi@noc.ac.uk

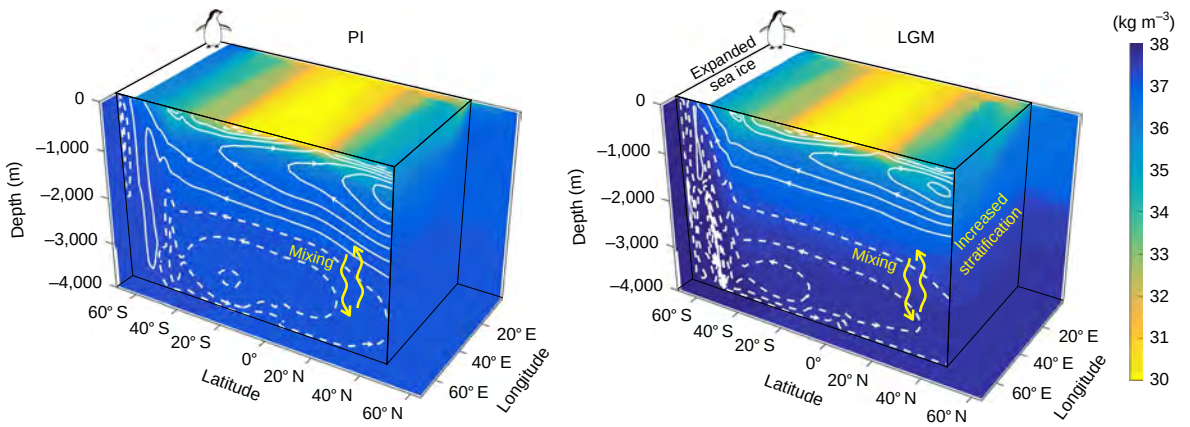

Fig. 1 | Changes in ocean circulation and sea ice cover between the PI and LGM. Figures show potential density referenced to 2,000 m (shading) and meridional overturning streamfunction (contours; solid lines for positive values and dashed for negative ones) for the PI and LGM reference simulations. Note that 1,000 kg m^{-3} has been subtracted from the potential density values. Sea ice cover of 25% or more is shown at the southern end of the domain (top face).

Simulated glacial ocean circulation and carbon storage

In our ocean–sea ice simulations, a lowering of atmospheric temperature leads to an expansion of Antarctic sea ice cover and increased deep-ocean stratification, as compared to the pre-industrial (PI) reference simulation (Fig. 1), in agreement with LGM reconstructions[7,30]. The 'LGM-like' ocean circulation is also characterized by a shallower AMOC, further separated from the abyssal cell than in the 'PI-like' case (Fig. 1), again broadly consistent with the palaeoclimate record[5]. Changes in the deep ocean circulation and stratification have been attributed to enhanced brine rejection from Antarctic sea ice formation in a colder climate, which leads to increased abyssal stratification[18]. The larger abyssal stratification in turn leads to a shoaling of the AMOC[22]. In the LGM configuration, AABW is more isolated from the surface due to (1) weaker mixing with North Atlantic deep water (NADW) as a result of a shoaling of the interface between the upper and abyssal cells to a depth where turbulent vertical mixing is reduced[21,31] and (2) reduced air–sea gas exchange under expanded sea ice around Antarctica[13]. The change in sea ice and circulation is, therefore, likely to favour increased carbon sequestration in the glacial deep ocean.

We test the increased glacial carbon storage hypothesis by coupling the physical ocean–sea ice model[18] to a biogeochemistry model[32] and a well-mixed atmospheric box, which allows atmospheric CO_2 concentrations to adjust while total carbon is conserved[33]. Under glacial conditions, the dissolved inorganic carbon (DIC) concentration increases substantially in the deep ocean (Fig. 2b), as a consequence of cooling, sea ice expansion and circulation changes. This results in a drawdown of atmospheric CO_2 concentrations by 40 ppm from 278 ppm in the PI to 238 ppm in the LGM (Fig. 2 and Table 1), which corresponds to about half of the inferred glacial–interglacial variations[34].

To better understand the changes in the partitioning of carbon between the atmosphere and ocean, we diagnostically decompose the atmospheric CO_2 drawdown into different physical and biological contributions[25,35–37]. The most easily understood contribution is associated with the solubility pump[38,39], which reflects the dependence of CO_2 solubility on the ocean's temperature and (to a lesser extent) salinity. As the ocean becomes colder, it can dissolve more carbon, but this only explains about 16 of the 40 ppm of atmospheric p_{CO_2} drawdown between the PI and LGM reference simulations (Fig. 2 and Table 1).

The largest contribution instead is associated with a strengthening of the disequilibrium pump, which reflects the air–sea disequilibrium at the surface. The large air–sea disequilibrium in the LGM simulation results from the fact that the abyssal overturning circulation, which carries waters enriched in DIC by the biological pump, reaches the surface only under sea ice around Antarctica, where outgassing is strongly inhibited. As a result, the disequilibrium pump drives a reduction of atmospheric CO_2 between the PI and LGM reference simulations of 39 ppm.

Some of the disequilibrium pump contribution, however, is offset by a reduction in the biological pump, which represents the export of carbon into the deep ocean via organic matter. The apparent weakening of the biological pump and an associated enhancement in the disequilibrium pump in the LGM simulation are probably related to changes in the AABW formation processes, and highlight some of the challenges in the interpretation of the carbon pump decomposition. In the present-day-like control simulation, convection at high southern latitudes does not fully reach the surface (not shown), but instead appears to be triggered by a subsurface cabbeling instability[40]. As a result, circumpolar deep water (CDW) is transformed into AABW with little direct surface exposure (although there is mixing between the CDW and surface waters). Because the diagnostic carbon pump decomposition only considers water that enters the surface model layer as ventilated, upwelling phosphate is not relabelled as preformed, which leads to an apparently efficient biological pump. In the LGM simulation, deep convection instead does reach to the surface, but CDW mostly comes to the surface under sea ice, where it is exposed to little air–sea gas exchange and relatively little biological production. However, any remineralized nutrients that come to the surface (even under ice) are relabelled as preformed, thus weakening the biological pump, while the associated DIC contributes to the disequilibrium pump. This highlights that compensating changes in the biological and disequilibrium pump need to be interpreted with caution, especially in the presence of sea ice. Nevertheless, our results highlight unambiguously that changes in sea ice and circulation in the colder climate more than double the CO_2 drawdown that would be expected from the solubility effect alone.

Sensitivity experiments

To illustrate the importance of Antarctic sea ice dynamics in explaining glacial atmospheric p_{CO_2} drawdown, we performed a sensitivity experiment where air–sea gas exchange and biogeochemistry do not depend on the sea ice cover (that is, the presence of sea ice is simply ignored in the computation of the air–sea flux of CO_2). The atmospheric CO_2 concentration in the PI simulation is virtually unaffected by this change, which may be understood by noting that the

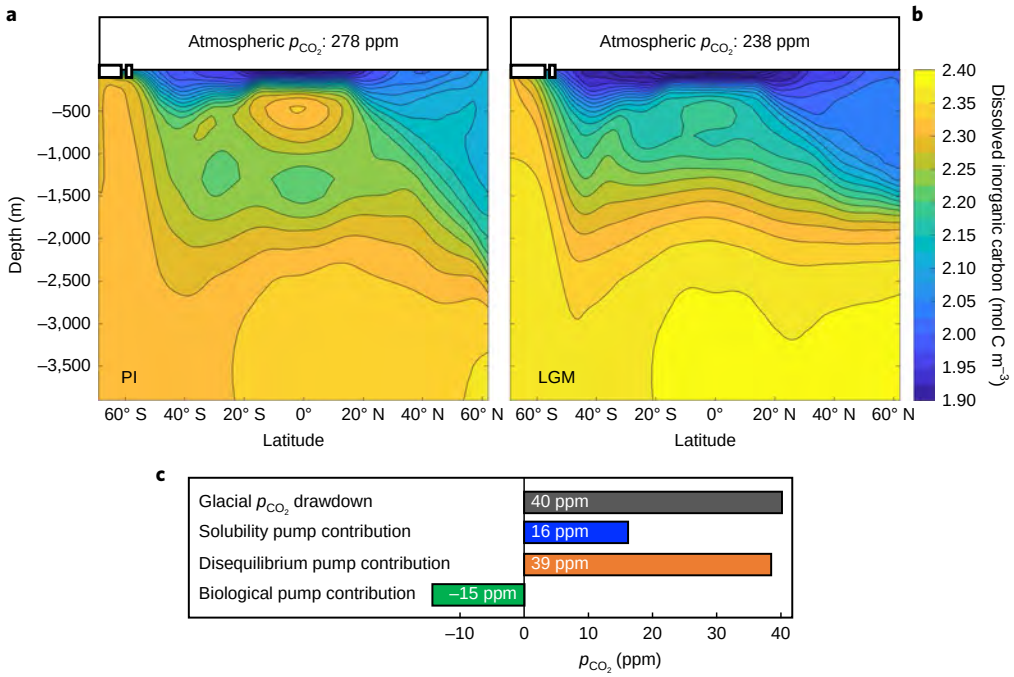

Fig. 2 | Deep ocean carbon storage and atmospheric CO_2 concentrations in the PI and LGM reference simulations. a,**b**, Zonally averaged dissolved inorganic carbon (DIC) for atmospheric CO_2 partial pressures, p_{CO_2}, of 278 ppm (**a**) and 238 ppm (**b**). Antarctic sea ice cover is sketched in white. **c**, The breakdown of the overall LGM p_{CO_2} change into different ocean carbon storage terms is shown for the reference simulation. The biological pump term includes contributions from both soft tissue and carbonate pumps, as well as the alkalinity effect of the latter (see Methods for more details). The distribution of the four components is shown and discussed further in the Supplementary Information (Supplementary Figs. 2 and 3).

abyssal cell is not as strongly isolated from the upper cell, such that not as much DIC can accumulate in the first place[21]. In the LGM simulation, the CO_2 concentration instead increases from 238 (in the LGM reference) to 268 ppm when the sea ice effect is removed, corresponding to a drawdown between PI and LGM of only 10 ppm (Table 1). The carbon pump decomposition indicates that the difference between the LGM simulation with and without sea ice effects on air–sea gas exchange is explained almost entirely by a change in the efficiency of the disequilibrium pump (Table 1). The mechanism for the drawdown of atmospheric p_{CO_2} here appears to differ from that described in ref. [27], which invokes a more efficient biological pump, driven by an increased residence time of waters near the surface, as opposed to a disequilibrium pump driven by suppressed air–sea gas exchange under sea ice in our case.

The important role of the disequilibrium pump is qualitatively consistent with the results of ref. [41]; however, contrary to our results, these authors suggest that sea ice is not a major driver of the disequilibrium pump. This may be a result of differences in the models used, but it may also arise from differences in the analysis. While we estimate the role of sea ice by eliminating the effect of sea ice on biogeochemistry in both PI and LGM experiments, their conclusion is based on sensitivity experiments using LGM sea ice cover in the PI simulation and vice versa. Prescribing LGM sea ice with PI ocean circulation does not account for the tight coupling between sea ice and circulation changes[17,18] and limits the drawdown potential, because the decoupling of the lower and upper cells and suppression of air–sea gas exchange need to act together to isolate the abyssal water masses[21].

Estimates of LGM circulation and carbon storage are expected to be sensitive to the vertical (that is, diapycnal) mixing rate, the magnitude of which is uncertain. The lower sea level would have significantly reduced the extent of shallow shelf seas, which probably led to enhanced tidal energy dissipation in the deep ocean, thus providing more energy for turbulent mixing[42,43]. At the same time, strongly enhanced deep ocean stratification, as predicted by our model, means that more energy is required to maintain a similar amount of vertical mixing[44]. As a result, the net change in mixing rates is uncertain. To test the sensitivity of LGM ocean carbon storage to changes in the vertical mixing rates in our model, we performed two sensitivity experiments where the diapycnal diffusivity was increased and reduced by 50%, respectively (Table 1). Increased diffusivity reduces carbon uptake in the LGM, which is consistent with the expectation that carbon sequestration in the deep ocean is less effective in the presence of strong vertical mixing[45]. Surprisingly, reduced mixing also leads to slightly reduced carbon uptake in the LGM, apparently as a result of a weaker biological pump (Table 1).

Changes in the disequilibrium pump, instead, are more robust: its contribution is increased with reduced diffusivity and decreased with enhanced diffusivity (Table 1), consistent with the expectation that water masses in the abyssal cell become increasingly isolated, mixing less with the relatively well-ventilated water masses of the upper cell. These results indicate that changes in the vertical mixing rate may have played an important role in the glacial carbon cycle, although the net effect on carbon storage is complex and may be sensitive to the specific magnitude and structure of vertical mixing—factors that are very hard to predict.

Although the focus of this study is on the physical drivers of ocean carbon storage associated directly with atmospheric cooling, it has often been suggested that changes in biological productivity, driven for example by changes in temperature, sea ice or dust fluxes, may also play a major role in explaining changes in p_{CO_2} between the present and LGM[2,46–48]. Although likely to be important, these feedbacks are relatively poorly understood and not included in our model. To address the potential role of changes in biological productivity in the context of our idealized LGM experiment, we explore the upper limit of biological carbon uptake by strongly increasing the maximum community production rate, such that virtually all available nutrients are consumed at the surface and the model approaches

Table 1 | Atmospheric p_{CO_2} (ppm) in the different PI and LGM simulations discussed in this study

	Control	$\kappa-50\%$	$\kappa+50\%$	No ice	Seasonal cycle	Max bio.
p_{CO_2} PI (ppm)	278			278	270	
p_{CO_2} LGM (ppm)	238	244	255	268	236	153
PI-LGM solubility pump (ppm)	16	20	16	17	15	12
PI-LGM biological pump (ppm)	−15	−42	−15	−16	5	122
PI-LGM disequilibrium pump (ppm)	39	57	22	10	14	−10

All experiments start from the same total carbon inventory as the PI reference simulation and have been integrated to equilibrium. The different contributions to the CO_2 drawdown between the PI and LGM simulations from the carbon pump decomposition are also shown for all simulations. For the LGM sensitivity experiments with reduced and increased vertical mixing, $\kappa-50\%$ and $\kappa+50\%$, respectively, as well as the LGM simulation with maximized biological productivity, 'max bio.', the CO_2 drawdown is computed relative to the PI control simulation. The DIC distribution in the sensitivity experiments is shown and discussed further in the Supplementary Information (Supplementary Fig. 1).

the maximum drawdown potential[49]. In this scenario, glacial p_{CO_2} concentrations decrease to 153 ppm, surpassing the reconstructed LGM values of ~180–190 ppm[34]. Enhanced biological productivity thus provides a possible pathway for a substantial CO_2 drawdown beyond the physical effects outlined here. In this experiment, the drawdown is strongly dominated by the biological pump (Table 1), as expected. By contrast, the disequilibrium pump contributes slightly negatively, because biological production rapidly utilizes the excess DIC in the upwelling waters and consequently removes the disequilibrium carbon in the mixed layer (especially around Antarctica). This result shows that physical and biological effects on ocean carbon storage are not linearly additive, illustrating the challenges in quantifying how different nonlinearly interacting mechanisms contribute to the observed lower CO_2 concentrations during the LGM.

The idealized simulations discussed so far do not include a seasonal cycle. Including seasonally varying temperatures in this model has been found to simulate significant seasonality in the sea ice cover around Antarctica, but only minor differences in the stratification and circulation[18]. Here, we test the effect of adding a seasonal cycle on the carbon cycle, using an additional sensitivity experiment with the same seasonal temperature forcing as in ref. [18]. The seasonal cycle is found to slightly reduce CO_2 concentrations in both PI and LGM simulations and, because the effect is somewhat stronger in the PI simulation, the PI-LGM CO_2 drawdown is slightly lower at 34 ppm (Table 1). As before, the CO_2 drawdown above the solubility pump effect is dominated by the change in the disequilibrium pump, although the latter is significantly weaker compared to the reference experiments without seasonality, but supported (rather than compensated) by a small increase in the biological pump. The difference in the decomposition of the CO_2 drawdown between the sets of simulations with and without seasonality primarily reflects differences in the PI simulations. Specifically, the PI experiment with a seasonal cycle has a weaker biological pump but stronger disequilibrium pump, probably due to differences in the details of AABW formation, which affect the decomposition into biological and disequilibrium pump contributions (as discussed in the context of the reference simulation above).

From atmospheric cooling to increased ocean carbon storage. Our results show that idealized ocean–ice biogeochemistry simulations forced solely by atmospheric cooling can not only reproduce inferred physical changes in the deep ocean circulation and stratification between the pre-industrial and last glacial climate, but also explain a substantial drawdown in atmospheric CO_2 concentrations. Although the specific numbers may need to be interpreted with caution because of the idealized model set-up, the key conclusion that sea ice dynamics and the associated circulation changes lead to an increase in glacial carbon drawdown well beyond the solubility effect alone is likely to be robust. The results, therefore, highlight the critical role of Antarctic sea ice in our understanding of glacial–interglacial transitions and that physical changes alone, triggered directly by atmospheric cooling, can provide a major contribution to the lowering of glacial atmospheric CO_2 concentrations. This would be consistent with the close coupling between CO_2 and Antarctic air temperatures, as observed in the ice core record[34].

Online content

Any methods, additional references, Nature Research reporting summaries, source data, statements of code and data availability and associated accession codes are available at https://doi.org/10.1038/s41561-019-0466-8.

Received: 19 July 2019; Accepted: 5 September 2019;
Published online: 14 October 2019

References

1. Sigman, D. M. & Boyle, E. A. Glacial/interglacial variations in atmospheric carbon dioxide. *Nature* **407**, 859–869 (2000).
2. Brovkin, V., Ganopolski, A., Archer, D. & Rahmstorf, S. Lowering of glacial atmospheric CO_2 in response to changes in oceanic circulation and marine biogeochemistry. *Paleoceanography* **22**, PA4202 (2007).
3. Marshall, J. & Speer, K. Closure of the meridional overturning circulation through Southern Ocean upwelling. *Nat. Geosci.* **5**, 171–180 (2012).
4. Marchitto, T. M., Oppo, D. W. & Curry, W. B. Paired benthic foraminiferal Cd/Ca and Zn/Ca evidence for a greatly increased presence of Southern Ocean Water in the glacial North Atlantic. *Paleoceanography* **17**, 10–11 (2002).
5. Curry, W. B. & Oppo, D. W. Glacial water mass geometry and the distribution of $\delta^{13}C$ of $\sum CO_2$ in the western Atlantic Ocean. *Paleoceanography* **20**, PA1017 (2005).
6. Lippold, J. et al. Strength and geometry of the glacial Atlantic meridional overturning circulation. *Nat. Geosci.* **5**, 813–816 (2012).
7. Adkins, J. F., McIntyre, K. & Schrag, D. P. The salinity, temperature, and $\delta^{18}O$ of the glacial deep ocean. *Science* **298**, 1769–1773 (2002).
8. Insua, T. L., Spivack, A. J., Graham, D., D'Hondt, S. & Moran, K. Reconstruction of Pacific Ocean bottom water salinity during the last glacial maximum. *Geophys. Res. Lett.* **41**, 2914–2920 (2014).
9. Wunsch, C. Pore fluids and the LGM ocean salinity reconsidered. *Quat. Sci. Rev.* **135**, 154–170 (2016).
10. Otto-Bliesner, B. L. et al. Last glacial maximum ocean thermohaline circulation: PMIP2 model intercomparisons and data constraints. *Geophys. Res. Lett.* **34**, L12706 (2007).
11. Muglia, J. & Schmittner, A. Glacial Atlantic overturning increased by wind stress in climate models. *Geophys. Res. Lett.* **42**, 9862–9868 (2015).
12. Marzocchi, A. & Jansen, M. F. Connecting Antarctic sea ice to deep-ocean circulation in modern and glacial climate simulations. *Geophys. Res. Lett.* **44**, 6286–6295 (2017).
13. Stephens, B. B. & Keeling, R. F. The influence of Antarctic sea ice on glacial–interglacial CO_2 variations. *Nature* **404**, 171–174 (2000).
14. Shin, S.-I. et al. A simulation of the last glacial maximum climate using the NCAR-CCSM. *Clim. Dyn.* **20**, 127–151 (2003).
15. Bouttes, N., Paillard, D. & Roche, D. M. Impact of brine-induced stratifi ation on the glacial carbon cycle. *Clim. Past* **6**, 575–589 (2010).
16. Watson, A. J. & Naveira Garabato, A. C. The role of Southern Ocean mixing and upwelling in glacial–interglacial atmospheric CO_2 change. *Tellus B Chem. Phys. Meteorol.* **58**, 73–87 (2006).
17. Ferrari, R. et al. Antarctic sea ice control on ocean circulation in present and glacial climates. *Proc. Natl Acad. Sci. USA* **111**, 8753–8758 (2014).
18. Jansen, M. F. Glacial ocean circulation and stratifi ation explained by reduced atmospheric temperature. *Proc. Natl Acad. Sci. USA* **114**, 45–50 (2017).
19. Sun, S., Eisenman, I. & Stewart, A. L. The influence of Southern Ocean surface buoyancy forcing on glacial–interglacial changes in the global deep ocean stratifi ation. *Geophys. Res. Lett.* **43**, 8124–8132 (2016).
20. Galbraith, E. & de Lavergne, C. Response of a comprehensive climate model to a broad range of external forcings: relevance for deep ocean ventilation and the development of late Cenozoic ice ages. *Clim. Dyn.* **52**, 653–679 (2019).

21. Nadeau, L.-P., Ferrari, R. & Jansen, M. F. Antarctic sea ice control on the depth of North Atlantic Deep Water. *J. Clim.* **32**, 2537–2551 (2019).
22. Jansen, M. F. & Nadeau, L.-P. The effect of southern ocean surface buoyancy loss on the deep-ocean circulation and stratifi ation. *J. Phys. Oceanogr.* **46**, 3455–3470 (2016).
23. Sarmiento, J. L. & Toggweiler, J. A new model for the role of the oceans in determining atmospheric pCO_2. *Nature* **308**, 621–624 (1984).
24. Archer, D. E. et al. Atmospheric pCO_2 sensitivity to the biological pump in the ocean. *Glob. Biogeochem. Cycles* **14**, 1219–1230 (2000).
25. Ito, T. & Follows, M. J. Preformed phosphate, soft tissue pump and atmospheric CO_2. *J. Mar. Res.* **63**, 813–839 (2005).
26. Kohfeld, K. E. & Ridgwell, A. Glacial–interglacial variability in atmospheric CO_2. *Surf. Ocean Low Atmosphere Process.* **187**, 251–286 (2009).
27. Watson, A. J., Vallis, G. K. & Nikurashin, M. Southern Ocean buoyancy forcing of ocean ventilation and glacial atmospheric CO_2. *Nat. Geosci.* **8**, 861–864 (2015).
28. Ganopolski, A. & Brovkin, V. Simulation of climate, ice sheets and CO_2 evolution during the last four glacial cycles with an Earth system model of intermediate complexity. *Climate* **13**, 1695–1716 (2017).
29. Ferreira, D., Marshall, J., Ito, T. & McGee, D. Linking glacial–interglacial states to multiple equilibria of climate. *Geophys. Res. Lett.* **45**, 9160–9170 (2018).
30. Gersonde, R., Crosta, X., Abelmann, A. & Armand, L. Sea-surface temperature and sea ice distribution of the southern ocean at the EPILOG last glacial maximum—a circum-Antarctic view based on siliceous microfossil records. *Quat. Sci. Rev.* **24**, 869–896 (2005).
31. Lund, D., Adkins, J. & Ferrari, R. Abyssal atlantic circulation during the Last Glacial Maximum: constraining the ratio between transport and vertical mixing. *Paleoceanography* **26**, PA1213 (2011).
32. Dutkiewicz, S., Follows, M. J. & Parekh, P. Interactions of the iron and phosphorus cycles: a three-dimensional model study. *Glob. Biogeochem. Cycles* **19**, GB1021 (2005).
33. Parekh, P., Follows, M. J., Dutkiewicz, S. & Ito, T. Physical and biological regulation of the soft tissue carbon pump. *Paleoceanogr. Paleoclimatol.* **21**, PA3001 (2006).
34. Petit, J.-R. et al. Climate and atmospheric history of the past 420,000 years from the Vostok ice core, Antarctica. *Nature* **399**, 429–436 (1999).
35. Goodwin, P., Follows, M. J. & Williams, R. G. Analytical relationships between atmospheric carbon dioxide, carbon emissions and ocean processes. *Glob. Biogeochem. Cycles* **22**, GB3030 (2008).
36. Lauderdale, J. M., Garabato, A. C. N., Oliver, K. I., Follows, M. J. & Williams, R. G. Wind-driven changes in Southern Ocean residual circulation, ocean carbon reservoirs and atmospheric CO_2. *Clim. Dyn.* **41**, 2145–2164 (2013).
37. Munday, D., Johnson, H. & Marshall, D. Impacts and effects of mesoscale ocean eddies on ocean carbon storage and atmospheric pCO_2. *Glob. Biogeochem. Cycles* **28**, 877–896 (2014).
38. Follows, M. J., Ito, T. & Marotzke, J. The wind-driven, subtropical gyres and the solubility pump of CO_2. *Glob. Biogeochem. Cycles* **16**, 1113 (2002).
39. Toggweiler, J., Gnanadesikan, A., Carson, S., Murnane, R. & Sarmiento, J. Representation of the carbon cycle in box models and GCMs: 1. Solubility pump. *Glob. Biogeochem. Cycles* **17**, 1026 (2003).
40. Foster, T. D. An analysis of the cabbeling instability in sea water. *J. Phys. Oceanogr.* **2**, 294–301 (1972).
41. Khatiwala, S., Schmittner, A. & Muglia, J. Air–sea disequilibrium enhances ocean carbon storage during glacial periods. *Sci. Adv.* **5**, eaaw4981 (2019).
42. Green, J. et al. Tidal mixing and the meridional overturning circulation from the Last Glacial Maximum. *Geophys. Res. Lett.* **36**, L15603 (2009).
43. Schmittner, A., Green, J. & Wilmes, S.-B. Glacial ocean overturning intensifi d by tidal mixing in a global circulation model. *Geophys. Res. Lett.* **42**, 4014–4022 (2015).
44. Wunsch, C. & Ferrari, R. Vertical mixing, energy and the general circulation of the oceans. *Annu. Rev. Fluid Mech.* **36**, 281–314 (2004).
45. Marinov, I. et al. Impact of oceanic circulation on biological carbon storage in the ocean and atmospheric pCO_2. *Glob. Biogeochem. Cycles* **22**, GB3007 (2008).
46. Mix, A. C. Influence of productivity variations on long-term atmospheric CO_2. *Nature* **337**, 541–544 (1989).
47. Kohfeld, K. E., Le Quéré, C., Harrison, S. P. & Anderson, R. F. Role of marine biology in glacial–interglacial CO_2 cycles. *Science* **308**, 74–78 (2005).
48. Martnez-Garca, A. et al. Iron fertilization of the subantarctic ocean during the last ice age. *Science* **343**, 1347–1350 (2014).
49. Ödalen, M., Nycander, J., Oliver, K. I., Brodeau, L. & Ridgwell, A. The influence of the ocean circulation state on ocean carbon storage and CO_2 drawdown potential in an Earth system model. *Biogeosciences* **15**, 1367–1393 (2018).

Acknowledgements

This work was funded by the National Science Foundation under awards nos. OCE-1536454 and OCE-1846821, and computational resources were provided by the Research Computing Center at the University of Chicago. A.M. received funding from NERC grant no. NE/P019293/1 (TICTOC).

Author contributions

A.M. and M.F.J. designed the study. A.M. performed the numerical simulations and analysed the results. A.M. and M.F.J. interpreted the results and wrote the manuscript.

Competing interests

The authors declare no competing interests.

Additional information

Supplementary information is available for this paper at https://doi.org/10.1038/s41561-019-0466-8.

Correspondence and requests for materials should be addressed to A.M.

Peer review information Primary Handling Editor(s): James Super, Rachael Rhodes.

Reprints and permissions information is available at www.nature.com/reprints.

Publisher's note Springer Nature remains neutral with regard to jurisdictional claims in published maps and institutional affiliations.

© The Author(s), under exclusive licence to Springer Nature Limited 2019

Methods

Ocean–sea ice model. The coupled ocean and sea ice model configur tion is the same as discussed in a previous manuscript[18], and uses the Massachusetts Institute of Technology ocean GCM (MITgcm[50]) in an idealized single-basin domain extending from 70° S to 65° N and covering 72° in longitude, with a re-entrant channel at the southern end of the domain (representing the Southern Ocean). The ocean has a uniform depth of 4 km, except for a sill in the Southern Ocean, which extends the continental barrier below 3 km depth. The horizontal resolution is 1°×1° and we use 29 vertical levels with varying thicknesses from 20 m at the surface to 200 m in the deep ocean. Diapycnal mixing is prescribed via a vertically varying profile, which is based on estimates of mixing driven by breaking internal waves[51]. The diffusivity values range from ~2×10^{-5} m^2 s^{-1} in the thermocline region to ~2×10^{-4} m^2 s^{-1} in the abyss[18]. Additional sensitivity experiments are performed where the diapycnal diffusivity has been reduced and increased by 50%. Mesoscale eddy effects are described via an eddy-driven overturning streamfunction[52] and along-isopycnal diffusion[53], with a variable eddy diffusivity[54]. The ocean component is coupled to a dynamic viscous-plastic sea ice model[55]. All atmospheric forcing fi lds are kept constant in time, with the exception of the sensitivity experiments including a seasonal cycle, where surface air temperatures vary every calendar month with the annual mean temperatures as in the other simulations[18]. Surface heat exchange restores the sea surface temperature to a prescribed zonally symmetric atmospheric temperature and salt fluxes are computed from a fi ed zonally symmetric profile of evaporation–precipitation[18]. A no-flux condition is applied at the bottom boundary; that is, geothermal heating is neglected. The changes in ocean circulation observed between the PI and LGM experiments do not appear to be sensitive to the details of the thermal boundary conditions[18], but additional details and sensitivity experiments are provided in ref. [18]. Crucially, the only difference in the boundary conditions between our PI and LGM simulations is a polar-amplifi d reduction in atmospheric temperatures, ranging from 2 °C in the tropics to ~6 °C at the poles, which is consistent with LGM proxy data (see ref. [18] and references therein).

Carbon cycle and atmosphere coupling. The ocean–sea ice component is coupled to an online biogeochemical model[32] that includes cycles of DIC, alkalinity, oxygen, phosphate and dissolved organic phosphorus. Different elements are linked by fixed Redfield stoichiometric ratios of R[C:N:P:O] = 117:16:1:−170 in biologically mediated transformations. Phosphate and light availability regulate the rates of carbon uptake and oxygen production by biological productivity, where phosphate consumption by biology is transformed into dissolved organic matter and the remaining portion sinks down as particulate organic matter; some fraction is not utilized and subducted as dissolved inorganic (or preformed) nutrients[32]. Calcium carbonate production is computed via a fixed rain ratio of 5% and carbonate chemistry is solved explicitly[56]. The air–sea exchange of CO_2 is parameterized with a gas transfer coefficient that depends on the square of the local wind speed[57]. Wind speed is computed based on the mean wind fields shown in ref. [18], to which we add a gustiness of 6.5 m s^{-1}, which leads to a global mean piston velocity of 20 cm h^{-1} (ref. [58]). A different value for the gas transfer coefficient was tested, in line with more recent estimates[59], but this made very little difference (not shown). In sea ice-covered regions, air–sea gas exchange is reduced by a factor representing the ice-covered fraction of the grid box (except for the sensitivity experiment where the effect of sea ice on air–sea fluxes is removed; Table 1).

The model is first integrated in the control configuration with pre-industrial boundary conditions, a prescribed atmospheric p_{CO_2} of 278 ppm and with initial values for alkalinity and DIC concentrations taken from ref. [24]. The model is integrated to equilibrium and the final state provides the initial conditions for all simulations discussed in the manuscript. The model is then coupled to an atmospheric box, which consists of a well-mixed carbon reservoir[33], so as to ensure conservation of the total amount of carbon; however, atmospheric CO_2 is not radiatively active, which means that there are no carbon cycle feedbacks on the rest of the simulated climate system. The mass of the atmosphere is scaled down to 4.9×10^{19} moles, so that the observed ratio between atmosphere and ocean mass is approximately equal to reality. All coupled ocean–ice–atmosphere simulations are again integrated to full equilibrium.

Carbon pump decomposition. The carbon pump is decomposed into various components with the help of explicit tracers for preformed phosphate and preformed alkalinity[60]. These tracers are reset to the local phosphate concentration and alkalinity at the surface, while being treated as passive tracers below. The alternative would be to extrapolate preformed alkalinity and phosphate using apparent oxygen utilization[29,36]; this leads to different results for the carbon pump decomposition (not shown) and may generate substantial overestimations and biases in the interpretation[41].

The preformed phosphate and alkalinity tracers allow us to separate the DIC in the ocean into components associated with the surface saturated carbon concentration C_{sat}, the soft tissue biological pump C_{soft}, the carbonate pump C_{carb} and the disequilibrium pump C_{dis}. C_{sat} can, at any point, be computed directly based on the temperature, salinity, preformed alkalinity and atmospheric p_{CO_2} using the carbonate chemistry equations[56]. C_{soft} is computed as

$$C_{soft} = 117(P - P_{pre}) \tag{1}$$

where P is the total phosphate and P_{pre} the preformed phosphate concentration. C_{carb} is computed as

$$C_{carb} = \frac{1}{2}[A_T - A_{pre} + 16(P - P_{Pre})] \tag{2}$$

where A_T is the in situ alkalinity and A_{pre} is the preformed alkalinity[36]. Finally, C_{dis} follows as

$$C_{dis} = DIC - C_{sat} - C_{soft} - C_{carb} \tag{3}$$

The separation of total DIC into C_{sat}, C_{soft}, C_{carb} and C_{dis} for the control PI and LGM simulations is shown in Supplementary Figs. 2 and 3. The results for the PI simulation are broadly consistent with previous studies[36,37,61], although the comparability to models and observations with a realistic continental configuration is limited by our single-basin geometry, where deep-ocean water masses share aspects with both the Atlantic and the Pacific. Comparison to observations is further limited by the indirect methods required to obtain the carbon pump separation from observable quantities and by the disequilibrium contribution associated with anthropogenic CO_2 uptake[61].

To attribute the atmospheric CO_2 drawdown to components associated with the different pumps, we consider the global carbon inventory[25,35]:

$$\Sigma C = Mp_{CO_2} + V[C_{sat} + C_{dis} + C_{soft} + C_{carb}] \tag{4}$$

Here ΣC is the total amount of inorganic carbon in the atmosphere and ocean, M is the molar volume of the atmosphere (4.9×10^{19} moles in our model) and V is the volume of the ocean (3.6×10^{17} m^3 in our model). Because the organic carbon contribution to the total carbon budget is negligible, ΣC is approximately constant, and changes in the various reservoirs between our pre-industrial and glacial simulations obey

$$\delta p_{CO_2} = \frac{V}{M}[\delta C_{sat} + \delta C_{dis} + \delta C_{soft} + \delta C_{carb}] \tag{5}$$

Ignoring nonlinearities, we can further decompose δC_{sat} into contributions associated with changes in temperature δC_T, salinity δC_S, preformed alkalinity δC_A and atmospheric CO_2 concentration itself δC_{CO_2} (ref. [36]):

$$\delta C_{sat} \approx \delta C_T + \delta C_S + \delta C_A + \delta C_{CO_2} \tag{6}$$

where

$$\delta C_T = \frac{\partial C_{sat}}{\partial T}\delta T,\ \delta C_S = \frac{\partial C_{sat}}{\partial S}\delta S,\ \delta C_A = \frac{\partial C_{sat}}{\partial A}\delta A,\ \delta C_{CO_2} = \frac{\partial C_{sat}}{\partial p_{CO_2}}\delta p_{CO_2} \tag{7}$$

Combining equations (5) and (6) and rearranging, we obtain

$$\delta p_{CO_2} = \alpha[\delta C_{sol} + \delta C_{dis} + \delta C_{bio}] \tag{8}$$

where $\alpha \equiv \left[M/V + \frac{\partial C_{sat}}{\partial p_{CO_2}}\right]^{-1}$, $\delta C_{sol} = \delta C_T + \delta C_S$ denotes the total change associated with the solubility pump, which here is dominated by the temperature effect (Supplementary Table 1), and $\delta C_{bio} = \delta C_{soft} + \delta C_{carb} + \delta C_A$ denotes the net effect of the biological pump. Here, changes in preformed alkalinity are driven primarily by the carbonate pump, which acts to increase the alkalinity gradient between the surface and the deep ocean. δC_A is therefore directly linked to the carbonate pump and overcompensates for the effect of δC_{carb}, such that a strengthening of the carbonate pump acts to raise atmospheric CO_2 concentrations[35]. Because the soft tissue and carbonate pumps are tightly linked in our model, we further combine them into a net biological pump contribution. Changes in the biological pump are generally dominated by the soft tissue pump with the net effect of the carbonate pump ($\delta C_{carb} + \delta C_A$) partially compensating in most cases (Supplementary Table 1).

The contributions of the solubility, disequilibrium and biological pumps to the total atmospheric p_{CO_2} change between the PI and LGM simulations are then defined as

$$(\delta p_{CO_2})_{sol} \equiv \alpha\delta C_{sol},\ (\delta p_{CO_2})_{dis} \equiv \alpha\delta C_{dis},\ (\delta p_{CO_2})_{bio} \equiv \alpha\delta C_{bio} \tag{9}$$

where α can either be computed directly or inferred from equation (8) as

$$\alpha = \frac{\delta p_{CO_2}}{\delta C_{sol} + \delta C_{dis} + \delta C_{bio}} \tag{10}$$

Here, we use equation (10), but either approximation leads to very similar results.

Data availability

The input files used to run the MITgcm simulations that support the findings of this study are available from the corresponding author upon request. The model output data for all simulations can be obtained from https://github.com/alicemarzocchi/MITgcmOutput.

Code availability

The MITgcm code is freely available for download at https://doi.org/10.5281/zenodo.1409237. Computer code used to process the model output and generate figures is available from the corresponding author on request.

References

50. Marshall, J., Hill, C., Perelman, L. & Adcroft, A. Hydrostatic, quasi-hydrostatic and nonhydrostatic ocean modeling. *J. Geophys. Res. Oceans* **102**, 5733–5752 (1997).
51. Nikurashin, M. & Ferrari, R. Overturning circulation driven by breaking internal waves in the deep ocean. *Geophys. Res. Lett.* **40**, 3133–3137 (2013).
52. Gent, P. R. & McWilliams, J. C. Isopycnal mixing in ocean circulation models. *J. Phys. Oceanogr.* **20**, 150–155 (1990).
53. Redi, M. Oceanic isopycnal mixing by coordinate rotation. *J. Phys. Oceanogr.* **12**, 1154–1158 (1982).
54. Visbeck, M., Marshall, J., Haine, T. & Spall, M. Specifi ation of eddy transfer coeffici ts in coarse-resolution ocean circulation models. *J. Phys. Oceanogr.* **27**, 381–402 (1997).
55. Losch, M., Menemenlis, D., Campin, J.-M., Heimbach, P. & Hill, C. On the formulation of sea-ice models. Part 1: Effects of different solver implementations and parameterizations. *Ocean Model.* **33**, 129–144 (2010).
56. Follows, M. J., Ito, T. & Dutkiewicz, S. On the solution of the carbonate chemistry system in ocean biogeochemistry models. *Ocean Model.* **12**, 290–301 (2006).
57. Wanninkhof, R. Relationship between wind speed and gas exchange over the ocean. *J. Geophys. Res. Oceans* **97**, 7373–7382 (1992).
58. Krakauer, N. Y., Randerson, J. T., Primeau, F. W., Gruber, N. & Menemenlis, D. Carbon isotope evidence for the latitudinal distribution and wind speed dependence of the air–sea gas transfer velocity. *Tellus B Chem. Phys. Meteorol.* **58**, 390–417 (2006).
59. Wanninkhof, R. Relationship between wind speed and gas exchange over the ocean revisited. *Limnol. Oceanogr. Methods* **12**, 351–362 (2014).
60. Ito, T. & Follows, M. J. Air–sea disequilibrium of carbon dioxide enhances the biological carbon sequestration in the southern ocean. *Glob. Biogeochem. Cycles* **27**, 1129–1138 (2013).
61. Williams, R. G. & Follows, M. J. *Ocean Dynamics and the Carbon Cycle: Principles and Mechanisms* (Cambridge Univ. Press, 2011).